J. Fluid Mech. (2009), *vol.* 624, *pp.* 255–279. © 2009 Cambridge University Press
doi:10.1017/S0022112008005430 Printed in the United Kingdom

Growth, oscillation and collapse of vortex cavitation bubbles

JAEHYUG CHOI[1]†, CHAO-TSUNG HSIAO[2],
GEORGES CHAHINE[2] AND STEVEN CECCIO[1]

[1]Department of Mechanical Engineering The University of Michigan, Ann Arbor, MI 48109-2121 USA
[2]DYNAFLOW Inc., Jessup, MD 20794 USA

(Received 11 August 2007 and in revised form 30 November 2008)

The growth, oscillation and collapse of vortex cavitation bubbles are examined using both two- and three-dimensional numerical models. As the bubble changes volume within the core of the vortex, the vorticity distribution of the surrounding flow is modified, which then changes the pressures at the bubble interface. This interaction can be complex. In the case of cylindrical cavitation bubbles, the bubble radius will oscillate as the bubble grows or collapses. The period of this oscillation is of the order of the vortex time scale, $\tau_V = 2\pi r_c/u_{\theta,max}$, where r_c is the vortex core radius and $u_{\theta,max}$ is its maximum tangential velocity. However, the period, oscillation amplitude and final bubble radius are sensitive to variations in the vortex properties and the rate and magnitude of the pressure reduction or increase. The growth and collapse of three-dimensional bubbles are reminiscent of the two-dimensional bubble dynamics. But, the axial and radial growth of the vortex bubbles are often strongly coupled, especially near the axial extents of the bubble. As an initially spherical nucleus grows into an elongated bubble, it may take on complex shapes and have volume oscillations that also scale with τ_V. Axial flow produced at the ends of the bubble can produce local pinching and fission of the elongated bubble. Again, small changes in flow parameters can result in substantial changes to the detailed volume history of the bubbles.

1. Introduction

The static pressure in the core of a linear vortex is depressed when compared with the pressure far from the vortex axis. In some cases, when the vortex circulation is large enough, the pressure in the vortex core can fall below the liquid vapour pressure, and it is possible for negative pressures, or tensions, to exist in the core. Vortex cavitation occurs when a small bubble or nucleus explosively grows when exposed to these liquid tensions in the vortex core. Sometimes vortex cavitation bubbles remain small compared with the vortex core radius, with nearly spherical rapidly growing and collapsing bubbles entirely within the confines of the vortex core. However, if the bubble is exposed to a prolonged or severe application of tension, the initially near-spherical bubble can expand and elongate to fill the core of the vortex and continue to grow along the vortex axis, becoming highly elongated. The growth, splitting and collapse of vortex cavitation bubbles can produce easily detectable sound pulses (Choi & Chahine 2004, 2007; Hsiao & Chahine 2005; Choi & Ceccio 2007).

---

† Email address for correspondence: choijh@umich.edu

Concentrated regions of vorticity often occur in the tip regions of lifting surfaces and in flows within and in the wake of turbomachines. Vortex cavitation is also a common feature of turbulent jets, wakes and shear layers. A comprehensive review is provided by Arndt (2002).

A recent series of experiments conducted by researchers at the University of Michigan and the US Navy's Naval Surface Warfare Center – Carderock Division illustrated some of the difficulties involved with the prediction and scaling of vortex cavitation inception and noise for flows induced by turbomachinery. The results of these studies are reported in Chesnakas & Jessup (2003), Oweis & Ceccio (2005) and Oweis *et al.* (2006*a*, *b*). In these studies, the location and inception pressure of the cavitation was associated with the presence of multiple interacting vortices. A variety of vortex–vortex interactions occurring with both co- and counter-rotating vortices of varying strength that can lead to the stretching of smaller vortex filaments, and these smaller vortices can produce cavitation at relatively high pressures due to both stretching of the vortices and the creation and modification of axial flow in the vortex cores. This phenomenon has been observed in the inception of jets and shear layers (Katz & O'Hern 1986; O'Hern 1990; Iyer & Ceccio 2002) and confirmed in advanced numerical simulations (Hsiao & Chahine 2004, 2008). Such flow complexities can make the scaling of vortex inception and noise in practical flows of turbomachinery problematic.

Typically, engineers would like to observe vortex cavitation with model scale experiments and then use these results to make predictions of behaviour at full-scale conditions. The above description of the vortex cavitation process suggests two potentially significant scale effects. First, the nuclei population on the model and full scale can differ substantially, leading to 'water quality' scale effects, and even if the two populations were the same, the different ratios between bubbles and core sizes will also result in scale effects. Second, the non-cavitating flow fields of the model and full-scale flows can differ, leading to 'Reynolds Number' scale effects. A simple example is the case of a single bubble in an isolated steady line vortex formed downstream of a hydrofoil. We can match the free stream pressure (or cavitation number) and the vortex circulation (or the lift coefficients of the two hydrofoils). But, the viscous core size of the two vortices will differ since their Reynolds number is different, and this will lead to a difference in minimum core pressures for the same free stream pressure. Thus, the inception potential for a given nucleus can vary between the two flows. The possible presence of multiple interacting vortices makes scaling even more challenging.

The detailed processes of vortex cavitation bubble inception, growth, splitting and collapse were originally considered in Chahine (1995) and recently examined in more details by Choi & Chahine (2004), Oweis, Choi & Ceccio (2004) and Hsiao & Chahine (2005). Choi & Ceccio (2007) examined individual cavitation vortex bubbles that were produced as laser-initiated nuclei passed through a region of pressure reduction and recovery. Figure 1 shows an example of the growth and collapse of an individual vortex cavitation bubble, along with the volume history and recorded noise emission. The results of this study revealed the sensitivity of the vortex bubble dynamics to relatively modest variations in the non-cavitating vortex properties (e.g. the vortex circulation and core size). The interaction between the growing nucleus and the surrounding vortical flow leads to changes in the pressure field surrounding the bubble and the subsequent bubble dynamics, and this leads to a wide variety of bubble volume histories.

This experimental examination of vortex bubble dynamics showed how changes in the initial nuclei size and vortical flow field could both influence the growth, collapse

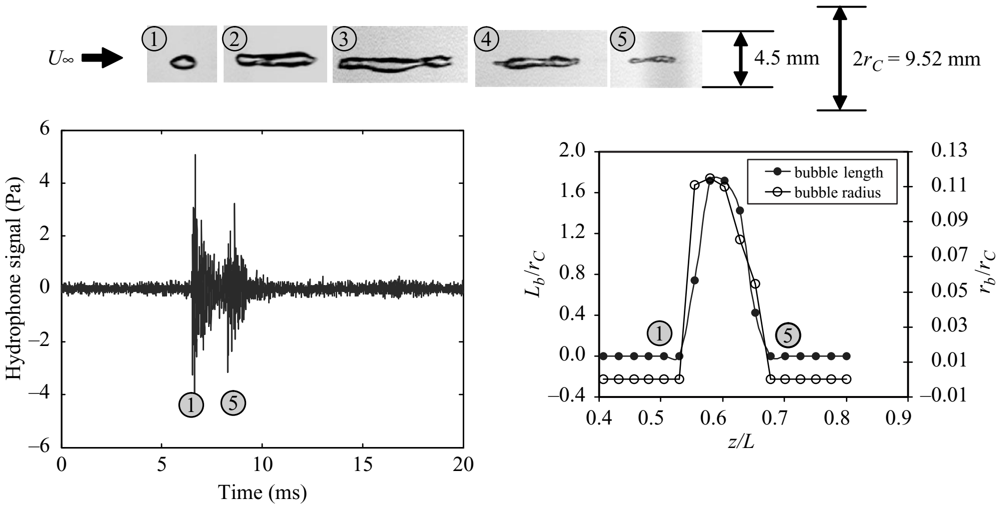

FIGURE 1. Typical images of the growth and collapse of an individual vortex cavitation bubble taking place over ∼ 3 ms and a bubble forms in the throat of a Venturi. The axial length and average radius of the bubble as a function of position within the Venturi are shown, along with the corresponding acoustic emission detected with a nearby hydrophone (Choi & Ceccio 2007).

and noise production of the vortex cavitation bubbles. In the present study, we use numerical simulations to examine the detailed flow interactions between the vortex cavitation bubble and the surrounding flow field, using a simplified two-dimensional analysis and an axisymmetric version of the code DF_UNCLE©. In doing so, our goal is to examine the underlying processes associated with water quality and Reynolds number scale effects during the growth and collapse of vortex cavitation bubbles. We will first consider the equilibrium radius of an elongated cavitation bubble. Then, we will consider the growth of a cylindrical nucleus. These idealized solutions will provide some insights into the more complex results obtained with the axisymmetric computations employing DF_UNCLE©.

2. Analysis of cylindrical vortex cavitation bubbles

2.1. *Background*

Before examining more complex bubble dynamics, we consider the equilibrium diameter of an elongated bubble that is growing along the axis of a line vortex. As we shall see below, the elongated bubble diameter is an important length scale of the flow, along with the core radius of the line vortex. The equilibrium diameter of a cylindrical bubble in a two-dimensional vortex was predicted analytically for a Rankine vortex model by Arndt & Keller (1992). They employed conservation of angular momentum to show that the radius of the cylindrical vapour bubble would be $r_b/r_C = 1/\sqrt{2}$ or 71 % of the initial core radius, and the viscous core would be replaced completely by vapour. However, experimentally observed cavitation bubbles were often significantly smaller in radius than the predicted value (Arndt 2002; Choi & Ceccio 2007). A similar analysis was conducted for a Gaussian vortex by Choi & Ceccio (2007). The original non-cavitating vortex has a profile given by the rotation velocity

$$u_\theta(r) = \frac{\Gamma_O}{2\pi r}\left(1 - \mathrm{e}^{-\alpha(r/r_C)^2}\right), \tag{2.1}$$

where Γ_O and r_C are the circulation and core size of the vortex, and $\alpha = 1.255$. We assume that there is no flow in the vortex axial direction. The pressure far from the vortex axis is P_∞, and the pressure at the axis, P_C, is given by

$$\frac{P_C - P_\infty}{\rho} = -\eta\left(\frac{\Gamma_O}{2\pi r_C}\right)^2, \tag{2.2}$$

where $\eta = 0.870$. The maximum tangential velocity is

$$u_\theta(r_C) = \beta\frac{\Gamma_O}{2\pi r_C}, \tag{2.3}$$

where $\beta = 0.715$. For Rankine vortex, $\eta = \beta = 1$ and $\alpha = 0$ outside of the viscous core. The cavitation number at the core of the vortex is defined by

$$\sigma_C = \frac{P_C - P_V}{(1/2)\rho(\beta\Gamma_O/2\pi r_C)^2} = \frac{P_\infty - P_V}{(1/2)\rho(\beta\Gamma_O/2\pi r_C)^2} - \frac{2\eta}{\beta^2}. \tag{2.4}$$

A given value of σ_C can be achieved by both changing the vortex properties (e.g. increasing the circulation or reducing the core size), or by reducing the free stream pressure. If $\sigma_C < 0$, the core will be in tension, and nuclei have the potential to grow. This local cavitation number was also introduced in Choi & Ceccio (2007), considering local axial velocity.

2.2. *Equilibrium model of cylindrical bubble growth*

We consider the flow field before and after a small bubble has grown and become highly elongated along the vortex axis, making the final flow essentially two-dimensional and the bubble a cylinder. The bubble will have modified the vortical flow, and the result need not be Gaussian. For this analysis, we will assume that the final flow field is Gaussian-like and is given by

$$u_{\theta,b}(r) = \frac{\Gamma_{O,b}}{2\pi(r - \gamma r_b)}\left(1 - \mathrm{e}^{-\alpha[(r-\gamma r_b)/(r_{Cb}-\gamma r_b)]^2}\right), \tag{2.5}$$

where $\Gamma_{O,b}$, r_{Cb} and γ are parameters of the cavitating vortex, and r_b is the cylindrical bubble radius. The parameter γ can vary in the range $0 < \gamma < 1$. The tangential velocity at the bubble interface is given by

$$u_{\theta,b}(r_b) = \frac{\Gamma_{O,b}}{2\pi r_b(1-\gamma)}\left(1 - \mathrm{e}^{-\alpha[(r_b(1-\gamma)/(r_{Cb}-\gamma r_b)])^2}\right). \tag{2.6}$$

When $\gamma = 0$, the liquid velocity profile is the same as that of a single-phase vortex, where the maximum tangential velocity will occur at $r = r_C$, and vapour occupies the region $0 < r < r_b$. The tangential velocity at the bubble interface will then be finite with the value

$$u_{\theta,b}(r_b) = \frac{\Gamma_{O,b}}{2\pi r_b}\left(1 - \mathrm{e}^{-\alpha[(r_b/r_{Cb}])^2}\right). \tag{2.7}$$

Conversely, if $\gamma = 1$, the tangential velocity at the bubble interface is zero. The bubble content is vapour pressure and this prescribes a boundary condition on the bubble surface. The bubble interface is assumed to be without shear stress.

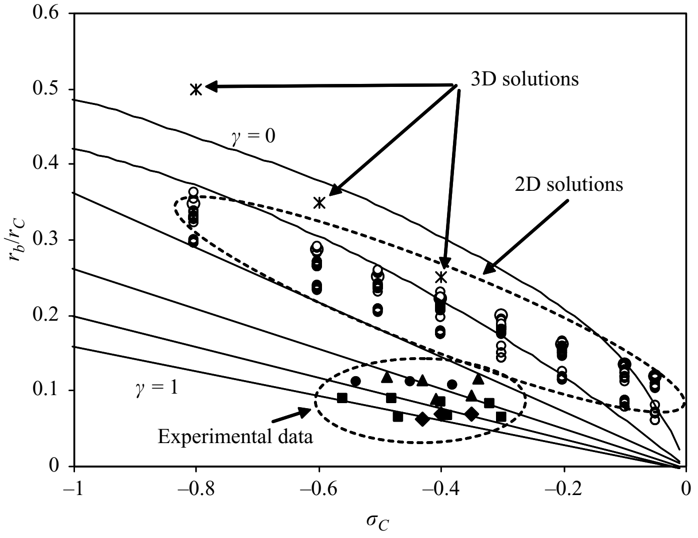

FIGURE 2. The calculated equilibrium radius of two-dimensional bubbles in the core of a two-dimensional Gaussian vortex for varying parameters, $\gamma = 0, 0.2, 0.4, 0.6, 0.8$ and 1.0. The solutions obtained from the dynamics of two-dimensional model are presented for the conditions of table 1 (O). Three-dimensional conditions are $Re_\Gamma = 2 \times 10^5(*)$ and $4 \times 10^5(+)$, with $\Delta T/\ \tau_v = 9.3$. Experimental data from Choi & Ceccio (2007) are also shown in filled symbols.

We need four relationships to close the problem. Conservation of angular momentum and the kinetic energy in the vicinity of the vortex with and without the bubble provide two relations. In addition, the Euler equation can be integrated to relate the pressure at the bubble interface to the pressure far from the vortex as follows:

$$\frac{P(r_b)-P_\infty}{\rho}=\frac{P_v-P_\infty}{\rho}=\int_\infty^{r_b}-\frac{1}{r}\left(\frac{\Gamma_{o,b}}{2\pi(r-\gamma\cdot r_b)}\left(1-\mathrm{e}^{-\alpha((r-\gamma\cdot r_b)/(r_{cb}-\gamma\cdot r_b))^2}\right)\right)^2\mathrm{d}r \tag{2.8}$$

The fourth parameter γ is a free parameter. Note that we assume that the pressure within the bubble is constant, and that oscillations of the bubble do not produce pressure gradients within the bubble. This simplification can be easily removed and a gas compression law can be added to account for the bubble dynamics as done in other studies using the same code (Hsiao & Chahine 2004, 2008).

The solution of these three relationships with varying values of γ will yield an envelope of possible vortex bubble radii. Figure 2 presents the resulting bubble radius as a function of cavitation number for a range of γ. Experimental data from Choi & Ceccio (2007) are also presented and are consistent with a value of $\gamma \sim 0.8$, suggesting that the circumferential velocity at the bubble interface is much reduced compared to the maximum rotation velocity in the liquid. The variation in the equilibrium r_b/r_C for different vortex conditions suggests that the tangential velocity that develops at the bubble interface may be a function of both the core radius and the vortex circulation, not simply the ratio $\Gamma_O/2\pi r_C$ that scales the non-cavitating core pressure. Also, this result suggests that the value of the tangential velocity at the bubble surface (related to γ in the model) may not be uniquely determined by the non-cavitating vortex properties but is the product of the detailed history of the initial bubble growth.

2.3. *Dynamic model of cylindrical bubble growth and collapse*

To explore this further, we consider the dynamics of a cylindrical bubble. The analysis presented here follows that of Chahine (1995) who examined the interaction of a bubble and a line vortex. Here, we consider a Gaussian vortex that has a *cylindrical* nucleus placed on its axis. The nucleus bubble is initially in pressure equilibrium, and a reduction in the far-field pressure will result in radial bubble growth. As the radius of the cylindrical bubble increases, it pushes away the surrounding liquid, redistributing the vorticity of the flow field. This, in turn changes the pressure near the bubble. This coupling of the radial bubble motion and the circumferential velocity field drives the infinitely long bubble dynamics, enabling us to assume two-dimensional behaviour.

$$\left(r_b\ddot{r}_b + \dot{r}_b^2\right)\ln\left(\frac{r_D}{r_b}\right) + \frac{r_b^2\dot{r}_b^2}{2}\left(\frac{1}{r_D^2} - \frac{1}{r_b^2}\right) = \frac{1}{\rho}\left(P_B - P_\infty\right) + \int_{r_b}^{r_D}\frac{u_\theta^2}{r}\,\mathrm{d}r, \tag{2.9}$$

where $r_b(t)$ is the radius of the bubble, P_B is the pressure in the liquid at the bubble surface and r_D is a given distance from the bubble axis. Introduction of r_D, where the far-field pressure is imposed, is needed to avoid singularity of the solution. This is a classical problem of two-dimensional bubble dynamics, which can be avoided more accurately by accounting for the liquid compressibility (e.g. Kedrinskii 2005). The use of a not too large r_D enables to recover a good approximate solution. The pressure far from the bubble is $P_\infty(t)$ and may be a function of time. The pressure within the cylindrical bubble is given by

$$P_B = P_V + P_G - 2\mu\frac{\dot{r}_b}{r_b} - \frac{S}{r_b}, \tag{2.10}$$

where S is the interfacial tension, and μ is the liquid viscosity. P_G is the pressure resulting from the presence of non-condensable gas in the bubble, which is usually assumed to have a polytropic relationship with the bubble volume

$$P_G = P_{GO}\left(\frac{r_O}{r_b}\right)^{2n}, \tag{2.11}$$

where r_O is the initial bubble radius and $n = 1$ for isothermal expansion or is equal to the ratio of specific heats for adiabatic expansion. Since the added mass of the expanding cylinder is infinite in an unbounded fluid, the first term in (2.9) becomes unbounded as $r_D \to \infty$. Nevertheless, it is instructive to examine the bubble dynamics resulting from these relationships for a finite, but large, value of r_D.

Franc & Michel (2004) present a solution for the dynamics of an oscillating cylindrical vortex bubble for the circumferential velocity distribution

$$u_\theta(r) = \frac{\Gamma_O}{2\pi r} r \geqslant r_b. \tag{2.12}$$

Here, the maximum tangential velocity occurs at the bubble surface and the length scale of the vortex core has been eliminated. The flow is assumed to be inviscid and without interfacial tension, and the bubble content is assumed to be vapour with a constant, P_V. When combined with (2.9), the equilibrium bubble radius r_b is found to be

$$\frac{\Gamma_O}{8\pi^2 r_b^2}\left[1 - \left(\frac{r_b}{r_D}\right)^2\right] = \frac{P_\infty - P_V}{\rho}. \tag{2.13}$$

The small-amplitude oscillation of the bubble radius about this equilibrium condition, for $r_D \gg r_b$, has a period

$$T = \frac{4\pi^2 r_b^2}{\Gamma_O}\sqrt{\ln\left(\frac{r_D}{r_b}\right)}. \tag{2.14}$$

Since the pressure in the bubble is assumed to be constant, the gas within the bubble does not contribute any stiffness. Instead, the radial motion of the bubble and the tangential velocity distribution are coupled to form a dynamic compliance. Increasing r_b will push the rotating fluid away from the axis, and angular momentum conservation will lead to a decrease in the average tangential velocity and an increase in the fluid pressure at the bubble interface, resisting the bubble's growth. Similarly, decreasing r_b will lead to a decrease in the local fluid pressure that will resist the bubble's further collapse. Hence, an oscillation can take place around an equilibrium radius.

The oscillation period is related to the time scale $4\pi r_b^2/\Gamma_O$, which is the time for a particle on the surface of the bubble to make one revolution. The period also has a logarithmic dependence on the radial extent of the domain, since the added mass of a cylindrical bubble becomes unbounded with increasing domain size. However, this solution illustrates the basic dynamics of the cavitating flow. The modified Rayleigh–Plesset equation (2.9) reveals that complex interactions may take place between the changing bubble radius, the surrounding rotating flow field and the resulting pressure field near the bubble wall. The exact relationship between $u_\theta(r, t)$ and $r_b(t)$ may not be simple, as these functions are coupled by the circumferential momentum equation and depend on the time history of the circumferential velocity distribution. If the bubble radius grows to the order of the original vortex core size, the velocity distribution may depart significantly from the modified Gaussian profiles assumed in the equilibrium analysis.

We will extend this analysis to examine the dynamic growth of a small cylindrical bubble in the core of a Gaussian vortex. We will consider the growth of the cylindrical bubble after the application of a pressure reduction in the far field, $\Delta P_\infty < 0$ over a period of time ΔT. The independent variables of the problem lead to the following non-dimensional parameters:

(*a*) The core cavitation number *before* the change in external pressure is set such that the original nucleus is in pressure equilibrium:

$$\sigma_{CO} = \frac{(P_{\infty O} - P_{BO})}{(1/2)\rho\,(\beta\Gamma_O/2\pi r_C)^2} - \frac{2\eta}{\beta^2} = 0, \tag{2.15}$$

where $P_{BO} = P_V + P_{GO} - S/r_b$.

(*b*) The core cavitation number after the application of the pressure reduction is

$$\sigma_C = \frac{(P_{\infty O} + \Delta P_\infty) - P_B}{(1/2)\rho(\beta\,\Gamma_O/2\pi r_C)^2} - \frac{2\eta}{\beta^2} = \frac{\Delta P_\infty}{(1/2)\rho(\beta\,\Gamma_O/2\pi r_C)^2}, \tag{2.16}$$

(*c*) The vortex Reynolds number is

$$Re_\Gamma = \frac{\rho\Gamma_O}{\mu}. \tag{2.17}$$

(*d*) The non-dimensional externally applied tension is

$$\frac{\Delta P_\infty}{P_{\infty O}} = \frac{\sigma_C\beta^2}{2\eta}\left[\frac{1}{1 + P_{BO}/\eta\rho(\Gamma_O/2\pi r_c)^2}\right]. \tag{2.18}$$

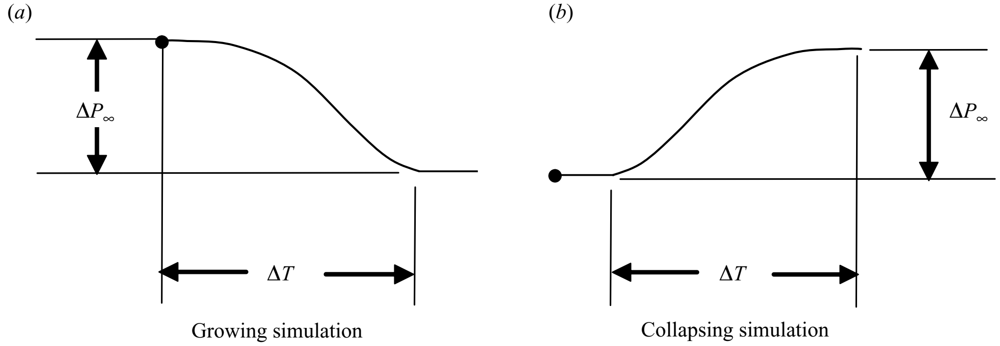

FIGURE 3. The pressure time history used in the simulation of driven bubble growth and collapse. The nucleus (cylindrical or spherical) starts at pressure equilibrium. Then, the pressure is reduced by ΔP_∞ over a period of time ΔT following a cosine function.

(*e*) The non-dimensional time over which the tension is applied is

$$\frac{\Delta T}{\tau_V} = \Delta T \frac{\beta \Gamma_O}{4\pi^2 r_c^2}, \tag{2.19}$$

where $\tau_V = 4\pi^2 r_c^2/\beta \Gamma_O$.

Examining (2.15), the minimum value of σ_C is $-2\eta/\beta = -3.40$ when the free-stream pressure is reduced to vapour pressure. Values of $0 > \sigma_C > -3.40$ can be achieved through a combination of the free-stream pressure and the vortex properties. Hence, for a fixed core tension, we may have different radial pressure gradients away from the vortex axis.

The dynamics of cylindrical vortex cavitation bubbles was examined over a range of applied pressures and pressure gradients. The amount of tension applied to the nucleus was set with σ_C, and the non-dimensional rate at which the pressure was applied is then $(\Delta P_\infty/\Delta T)(\tau_V/P_{\infty O})$. A small cylindrical nucleus of radius r_O is placed on the axis, and the initial external pressure $P_{\infty O}$ is set such that the liquid pressure at the surface of the nucleus is in equilibrium with the contents of the bubble and surface tension, and the presence of non-condensable gas is ignored. A fixed value of $r_O = 100$ μm was used along with the properties of room-temperature water.

The continuity equation and the Navier–Stokes equations in the radial and circumferential directions were solved for axisymmetric bubble growth. The motion of the bubble wall was coupled to the flow field, capturing the interaction between $u_\theta(r, t)$ and $r_b(t)$. The radial and tangential mass conservation and Navier–Stokes equations were solved with a fourth-order Runge–Kutta scheme for each time step. Space was discretized using 10 000 radial points between $r = 0$ and $100 r_C$. The time steps did not exceed $0.001\tau_V$. A time varying pressure, shown in figure 3, was imposed on the boundary at $r = 100 r_C$. A series of computations were performed with increasing domain size to determine when the solution variations from domain size to the next started varying very little, even though the analytical solution suggests that true independence cannot be reached. The data of figure 4 suggest that a $100 r_D/r_C$, domain size may be sufficiently large to eliminate strong dependence on domain size. One should note than in this figure between $5 r_D/r_C$ and $1000 r_D/r_C$ the variations of r_b/r_C are less than by 1 %.

A series of computations were performed to examine the dynamic behaviour of the cylindrical vortex cavitation bubble. The vortex properties, applied tension and rate of pressure reduction were all varied, and the conditions are shown in table 1.

Γ_0 ($\mathrm{m^2\,s^{-1}}$)	r_C (mm)	$\Delta T/\tau_v$		
		0.5	1	2
0.1	1	$9\times\sigma_C$	$9\times\sigma_C$	$9\times\sigma_C$
	2			
0.4	4	$9\times\sigma_C$	$9\times\sigma_C$	$9\times\sigma_C$
	8			
2.0	20	$9\times\sigma_C$	$9\times\sigma_C$	$9\times\sigma_C$
	40			

TABLE 1. The matrix of parameters used in the two-dimensional dynamic bubble simulations. $\sigma_C=\Delta P_\infty/(1/2\rho u^2_{\theta,max})$ and has the values $\sigma_C=0.05$, -0.10, -0.20, -0.40, -0.50, -0.60, -0.80, -1.00. ΔP_∞ is the reduction in pressure applied to the bubble over the time, ΔT. The maximum tangential velocity of the vortex before growth of the cavitation bubble is $u_{\theta,max}$ and occurs at the core radius r_C. $\tau_v=2\pi r_C/u_{\theta,max}$ is the vortex time scale.

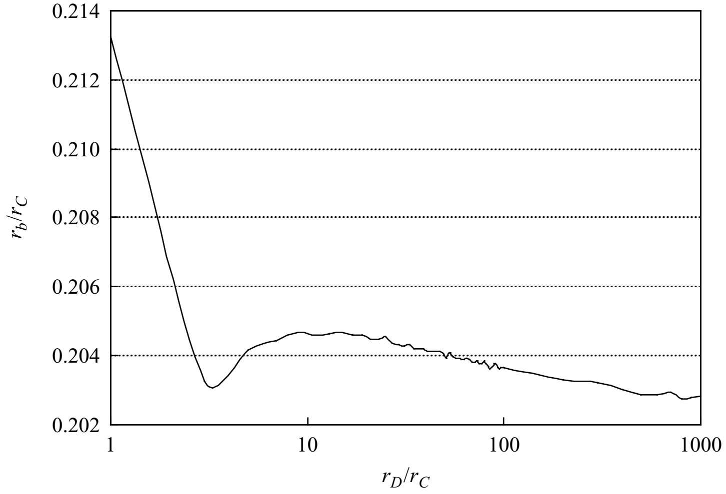

FIGURE 4. Convergence of the equilibrium bubble radius computed with the dynamic two-dimensional model as a function of the domain size r_D/r_C. Here, $\sigma_C=-0.4$.

In this way, the influence of these parameters on the bubble dynamics and the elongated bubble radius were revealed. Figure 5 presents typical time histories of the bubble growth for varying levels of applied tension. Once the cylindrical nucleus begins to grow, oscillations of the bubble radius begin. After the application of the tension is complete, the radius oscillates about a mean value, and the oscillations are approximately sinusoidal. We can compare the mean radius of the bubble after the tension has been applied with the results of the equilibrium model, as shown in figure 2. The average equilibrium radius of the cylindrical bubble falls within the envelope of the data computed with the quasi-static model. The fully coupled cylindrical bubble/viscous flow data suggest that the growth of the cylindrical bubble leads to high tangential velocities at the bubble surface, and hence, to a lower value of γ.

The amplitude of the radial oscillations grows with the magnitude of the applied tension as shown in figure 5(*a*), and also grows with the rate of application of the tension as shown in figure 5(*b*). Also, note that the rate of the applied tension does not significantly influence much the final average bubble radius. At the Reynolds numbers

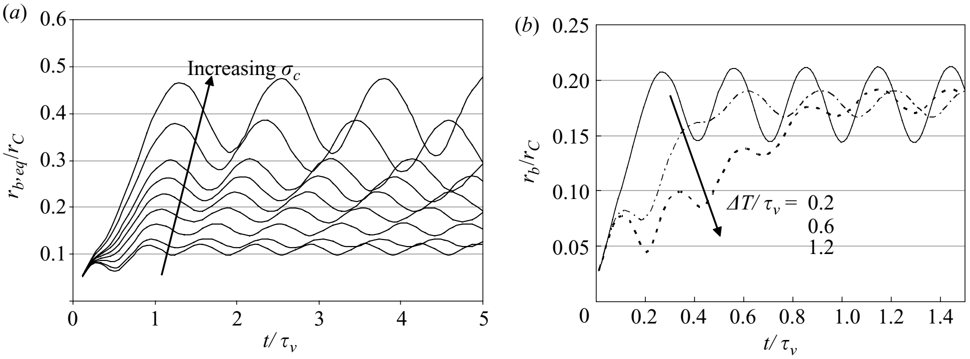

FIGURE 5. (a) Growth of the two-dimensional bubble as a function of time for $\Gamma_0 = 0.2$, $r_C = 4$ mm, with $\Delta T/\tau_v = 1.0$. The results for nine cavitation numbers are shown $\sigma_C = 0.05$, -0.10, -0.20, -0.40, -0.50, -0.60, -0.80, -1.00; (b) Growth of the bubble for $\sigma_C = -0.3$, with $\Delta T/\tau_v = 0.25$, 0.60 and 1.20.

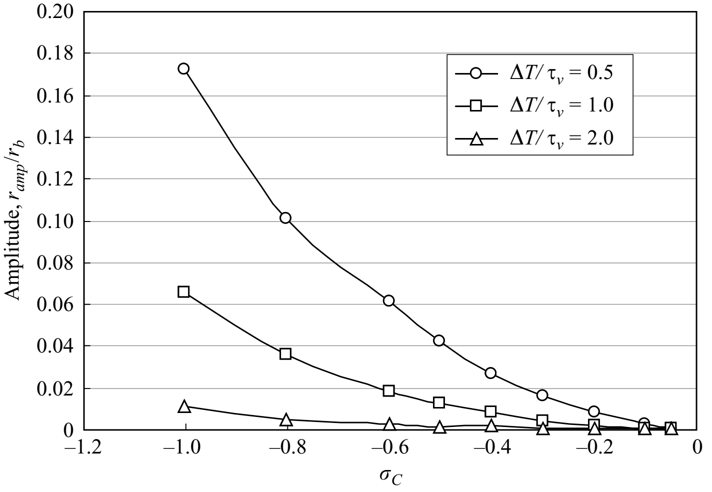

FIGURE 6. The amplitude of the near-sinusoidal radial bubble oscillations of the two-dimensional bubbles after the initial growth phase has been completed. Results are shown for varying cavitation numbers for three different values of $\Delta T/\tau_v = 0.5$, 1.0 and 2.0. $\Gamma_0 = 0.1$, $r_C = 1$ mm.

considered here, the viscous damping of the flow is relatively small, and the radial oscillations continue without a noticeable decay in amplitude. The amplitude of these radial oscillations is strongly related to the magnitude and the rate of the applied tension, with the ratio of the amplitude to the mean bubble radius becoming larger as the tension is increased, as shown in figure 6. The amplitude was not observed to depend on Reynolds number over the range of parameters examined.

The normalized period of the radial oscillations also grows with an increase in magnitude of the applied tension, as shown in figure 7. The oscillation frequency decreases with increasing equilibrium bubbles size and the applied tension increases, but it appears to be unaffected by changes in the Reynolds number or by the rate at which the tension is applied. The non-dimensional period $T\beta\Gamma_O/4\pi^2 r_c^2$ is between 0.6 and 1.4 times the vortex time scale. The analytical solution for the period of

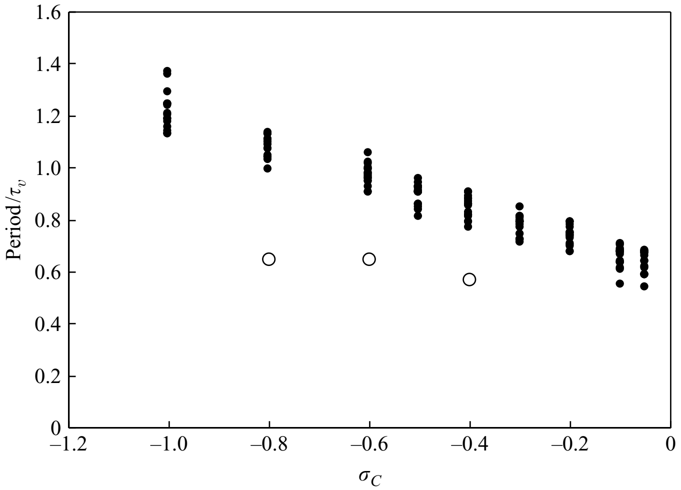

FIGURE 7. The period of the near-sinusoidal radial bubble oscillations of the two-dimensional bubbles after the initial growth phase has been completed. All the conditions in table 1 are shown, and the solid symbols represent two-dimensional simulation results. Three-dimensional bubble simulation at $\Delta T/\tau_v = 3.7$ (O). Both conditions are at $\Gamma_0 = 0.2$, $r_C = 4$ mm.

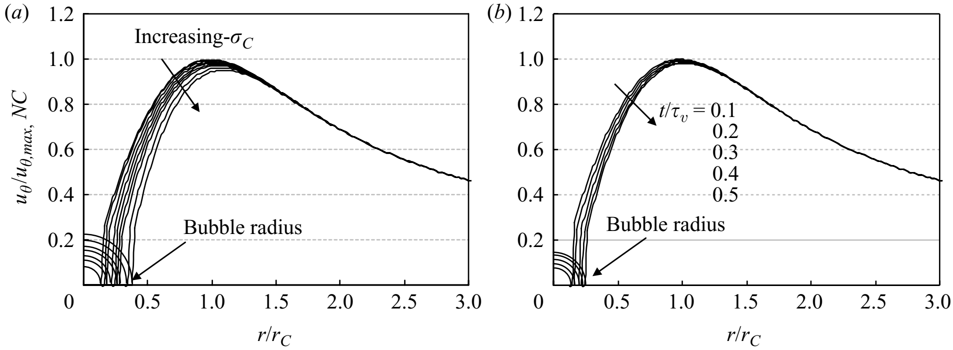

FIGURE 8. The modified circumferential velocity profile of the vortical flow during the growth of the two-dimensional bubbles corresponding to $\Gamma_0 = 0.1$, $r_C = 1$ mm and (a) $\Delta T/\tau_v = 0.5$ and $t/\tau_v = 1$ for varying σ_C (b) $\sigma_C = -0.4$ and $\Delta T/\tau_v = 0.5$ for varying times $t/\tau_v.u_{\theta,max,NC}$ is the maximum tangential velocity for non-cavitating vortex.

the oscillating cylindrical bubble (2.14) shows that the period should increase with increasing domain size by a factor of $\sqrt{\ln(r_D/r_b)}$. For the domain size chosen here, $2.3 < \sqrt{\ln(r_D/r_b)} < 2.7$, and $1.6 < T\beta\Gamma_O/[4\pi^2 r_c^2\sqrt{\ln(r_D/r_b)}] < 3.3$. The scaling expressed in (2.18) suggests that the bubble growth will be influenced by variations in the radial pressure gradients near the bubble that would occur, say, for two vortices with the same core cavitation number but different Reynolds number. However, these differences in the pressure gradient did not lead to noticeable differences in the bubble growth over the range of parameters examined here.

The growth of the cylindrical bubble modifies the vortical flow field and changes the radial velocity profile. Figure 8(a) presents the circumferential velocity profile during bubble growth for $\Gamma_0 = 0.1$, $r_C = 1$ mm and $\Delta T/\tau_v = 0.5$ for varying $\sigma_C = -0.4$ at time $t/\tau_v = 1$, and figure 8(b) presents the velocity profiles for various t/τ_v at

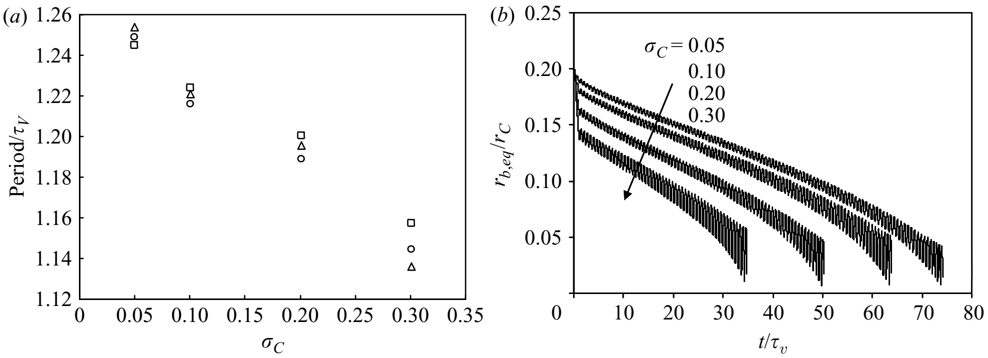

FIGURE 9. Behaviour of a two-dimensional bubble during the collapse process: $\Gamma_0 = 0.2$, $r_C = 2$ mm. (*a*) The period of the near-sinusoidal radial bubble oscillations of the two-dimensional vortex cavitation bubbles. The symbols represent different rates of applied tension. $\Delta T/\tau_v = 1$ (○), 2.5 (□) and 5(△). (*b*) Collapse of steady and oscillating two-dimensional cavitation bubbles at $\Delta T/\tau_v = 2.5$ for varying σ_C: $\sigma_C = 0.05$, 0.1, 0.2 and 0.3.

fixed σ_C. The circumferential velocity profiles are displaced by the growing bubble and result in a lower peak circumferential velocity of the flow, and the reduction in the peak circumferential velocity is an expected consequence of angular momentum conservation. The circumferential velocity near the bubble interface remains low with large modification of the vortical flow field and remains near zero when $\gamma = 1$.

The collapse of a cylindrical bubble in a vortex line was also examined. Figure 9 presents the collapse of cylindrical bubbles, which were initially steady, subjected to the pressure profile shown in figure 3(*b*) and for various σ_C. Bubble oscillations are observed during the collapse with a nearly constant frequency of oscillation. This frequency is weakly related to the rate at which the increase in pressure is applied $\Delta T/\tau_v$ as shown in figure 9(*a*). Increasing the applied pressure increases the rate at which the bubble collapses, as shown in figure 9(*b*). We can compare the collapse time of the bubble to that of a spherical bubble in a quiescent liquid. In this case, the collapse time scales as $\tau_{CS} \sim r_b/\sqrt{\rho/\Delta P}$. The ratio of this time scale to that of the vortex τ_v is given by $\tau_{CS}/\tau_v \sim (r_b/r_C)/(\pi\sqrt{2\sigma_C})$ and is between 0.1 and 0.2 for the parameters considered here. Figure 9(*b*) shows that, after an initial sudden decline in the bubble radius, the time to full collapse is two orders or magnitude larger than that of the spherical bubble. As the cylindrical bubble collapses, the average driving pressure difference is reduced, and hence a much longer time is taken before complete collapse.

Both the equilibrium and dynamic simulations of the cylindrical bubbles suggest that modification of the surrounding vortical flow by the expanding bubble strongly influences the ultimate radius that the bubble will achieve. Also, the dynamic model illustrates how these flow interactions can lead to radial bubble oscillations. Next, we will examine the dynamics of more realistic bubbles that can grow and oscillate in both the radial and axial directions of the vortex.

3. Three-dimensional calculation using DF_UNCLE©

3.1. *Background*

A three-dimensional unsteady Navier–Stokes solver has been developed by DYNAFLOW, Inc. for the simulation of complex bubble dynamics (Hsiao & Chahine

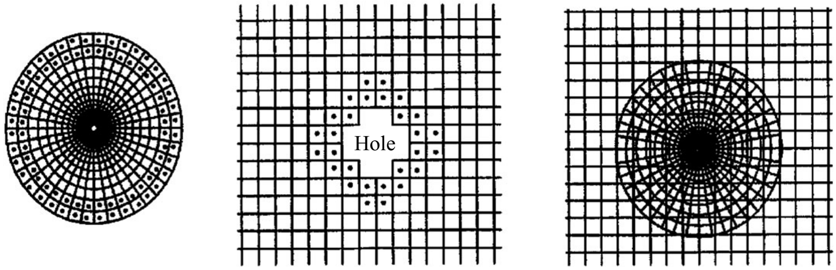

Sub grid Global grid Overall grid

FIGURE 10. Two-dimensional illustration of a Chimera grid system and localization of the hole and of the overlap points marked with a solid dot (Hsiao *et al.* 2004).

2001, 2004, 2008), and a summary of the method is provided here. The three-dimensional incompressible Navier–Stokes flow solver, DF_UNCLE$^{\copyright}$ is modified from the unsteady Navier–Stokes equation solver (UNCLE) developed at Mississippi State University (Arabshahi, Taylor & Whitfield 1995) to include bubble, cavity and free-surface effects. The numerical scheme of DF_UNCLE$^{\copyright}$ is a finite volume formulation. To investigate the bubble dynamics a Chimera grid scheme moving with the bubble was adopted with free-surface boundary conditions, as illustrated in figure 10. The Navier–Stokes equations are solved for the global and subgrids, and interpolation work is performed for overlapping these two grids. In order to consider nuclei growth and capture by the vortex prior to the conditions where non-spherical behaviour becomes predominant, a spherical bubble model is adopted, which uses a modified Rayleigh–Plesset equation based on a bubble surface-averaged pressure (SAP) for the pressure driving the bubble dynamics. This model was developed by Hsiao & Chahine (2001) and used by Choi, Hsiao & Chahine (2004) and Choi & Chahine (2007). Once bubble vortex interaction is significant and the bubble radius starts increasing, the DF_UNCLE$^{\copyright}$ non-spherical model with a subgrid is used to solve the Navier–Stokes equations including full bubble flow field interaction. Balance of the normal stress and tangential stress is enforced as boundary conditions on the bubble interface, and the motion of the bubble interface is fully coupled with the liquid flow field.

First, the growth and collapse of a cavitation nucleus placed on the axis of a liquid vortex was examined. The non-cavitating vortical flow consisted only of a circumferential velocity distribution (i.e. no axial or radial flows). An O–O type three-dimensional, spherical grid domain ($41 \times 21 \times 25$) was generated as a spherical subgrid for the bubble using 41×21 grid points on the bubble surface, and an H–H type rectangular grid ($61 \times 31 \times 31$) was used for the flow field. There were 16 grid points across the core of the vortex before the nucleus began to grow significantly. To have finer grids near the bubble liquid interface, a stretched grid spacing scheme was adopted. The rectangular domain had a size of $3 \times r_C$ by $10 \times r_C$ and the size of the bubble grid domain, which stretched with the bubble size during the simulation, was 30 times the instantaneous effective bubble radius ($\mathrm{R}_{eff} = (3V_b/(4\pi))^{1/3}$). The bubble was re-gridded during the simulation to maintain the original grid stretching factors and obtain good spatial resolution. Figure 11 shows the overlapped spherical grid and rectangular grid domains in the three-dimensional field. Finally, we constrained the solution to be axisymmetric. The pressure and tangential velocity of the undisturbed vortex were prescribed at the axial boundaries of the domain, even though it is

$\Delta T/\tau_v$	Re_Γ		$\Delta T/\tau_v$		Re_Γ	
	2×10^5	4×10^5			2×10^5	4×10^5
Small	$3\times\sigma_C$	$3\times\sigma_C$	Small	$2\times\sigma_C$	$3\times L_b/D_b$	$3\times L_b/D_b$
Middle	$3\times\sigma_C$	$3\times\sigma_C$	Middle	$2\times\sigma_C$	$3\times L_b/D_b$	$3\times L_b/D_b$
Large	$3\times\sigma_C$	$3\times\sigma_C$	Large	$2\times\sigma_C$	$3\times L_b/D_b$	$3\times L_b/D_b$

TABLE 2. The matrix of parameters used in the three-dimensional dynamic bubble simulations. $\sigma_C = \Delta P_\infty/(1/2\rho u^2_{\theta,max})$ and has the values $\sigma_C = -0.4$, -0.6 and -0.8 for the growing bubbles, and $\sigma_C = 0.4$ and 0.6 for the collapsing bubbles, ΔT. The maximum tangential velocity of the vortex before growth of the cavitation bubble is $u_{\theta,max}$ and occurs at the core radius, r_C. $\tau_v = 2\pi r_C/u_{\theta,max}$ is the vortex time scale. For the collapse cases, the ratio of the mean length L_b and diameter D_b, before collapse is varied.

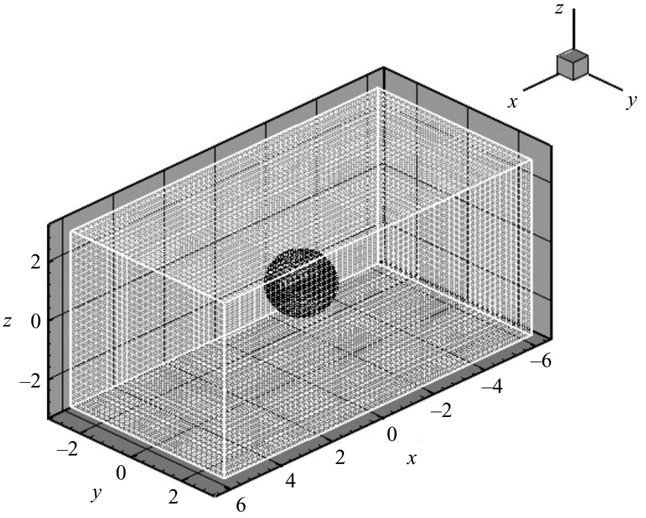

FIGURE 11. Grid domain used in the axisymmetric simulations. A total of $41\times21\times21$ grid points are specified to generate the spherical subgrid for the bubble, with 41×21 grid points used on the bubble surface. For the rectangular overall grid, a total of $61\times31\times31$ grid points are used.

possible to have velocity gradients at the boundary. To simulate both the growth and collapse of bubbles, the static pressure at the radial extent of the domain was prescribed and was varied with time as illustrated in figure 3. The time step for the simulation was chosen to be in the range $0.001 < r_C/u_{\theta,M} < 0.005$.

The growth and collapse of the bubble was computed for various pressure histories, growth and collapse times and bubble aspect ratios, detailed in table 2. The Reynolds number ($Re_\Gamma = \Gamma_O/\nu$) was also varied by doubling the vortex core size while maintaining the same initial maximum tangential velocity. Collapse bubble simulations were performed for bubbles with varying initial mean length to diameter ratios L_b/D_b. Fission of the bubbles was assumed to occur when the local radial distance between two points of the bubble became smaller than the grid size at the bubble interface. The results of the simulations were non-dimensionalized using the vortex core radius as the length scale and the vortex time scale. In physical coordinates, the simulated core radius was 4 and 8 mm, depending on the scale of

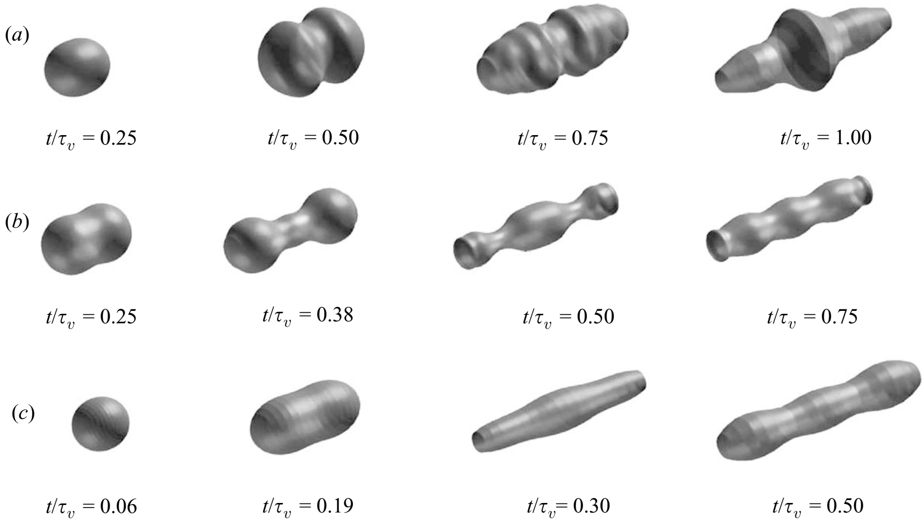

FIGURE 12. Volume history of three-dimensional bubbles in a line vortex during bubble growth for (*a*) $Re_\Gamma = 2 \times 10^5$ and $\sigma_C = -0.4$, for and $\Delta T/\tau_v = 0.46$ (*b*) $\Delta T/\tau_v = 1.13$. Also shown is the volume history for (*c*) $Re_\Gamma = 4 \times 10^5$ and, $\sigma_C = -0.4$, and $\Delta T/\tau_v = 0.23$.

the given vortex ($Re_\Gamma = 2 \times 10^5$ and 4×10^5), and the maximum tangential velocity was 5.7 m s^{-1}. The non-dimensional time scale τ_v was 4.42 and 8.84 ms in this study. Transition from the SAP model to the non-spherical model was imposed when $r_{b,eq}$ exceeded 200 μm.

3.2. *Vortex bubble growth from a spherical nucleus*

The growth of bubbles in a vortex from an initially spherical nucleus into an elongated bubble was examined. Figure 12 presents images of the growing bubble in the vortex for fixed Reynolds number and applied tension, with two different rates of application of the tension. Figure 13 presents the bubble radius and length as a function of time for the different conditions. The radius and length of a cylinder with the same volume of the elongated bubble are plotted. Unlike the cylindrical bubble growth discussed above, in these numerical simulations the small spherical nucleus grows simultaneously in the axial and radial directions until it becomes elongated. However, there are some significant similarities. The radius that the bubble achieves increases with increasing tension, and the radius oscillates with a period that is of the order of the vortex time scale. However, the bubble cannot grow monotonically in the axial direction. Instead, the radial extent of the bubble also oscillate until it, possibly, achieves an equilibrium rate of axial growth. Figure 14 presents close-up views of the flow field near the axial extent of the bubble in a plane containing the axis of the bubble. A flow generated from the axial growth of the bubble moves around the bubble tip and towards the middle of the elongated bubble, demonstrating how the radial and axial bubble motions become coupled through local modification of the bubble surrounding flow field and resulting in an abrupt change of the bubble shape and the formation of a re-entrant jet. Recall that in these simulations, the pressure inside the elongated bubble is essentially constant at the vapour pressure, so there is no dynamics due to changes in the internal bubble pressure. (These effects can also be simulated but were not considered here.) The radial motion of the bubbles can include oscillation, growth, collapse and rebound phases, when the flow generated by

(a) $Re_\Gamma = 2 \times 10^5$, $\Delta T/\tau_v = 0.46$

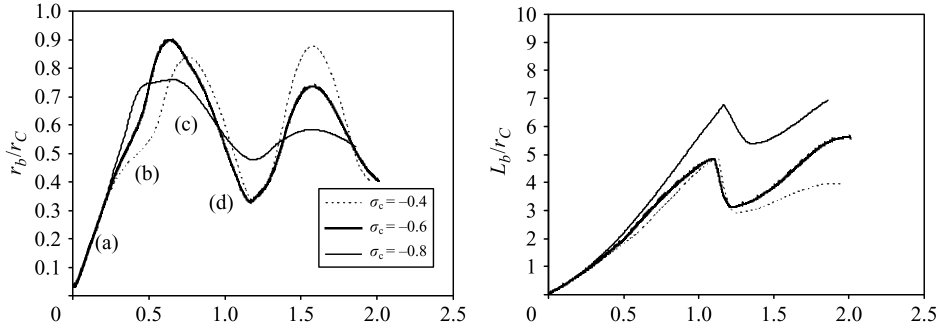

(b) $Re_\Gamma = 2 \times 10^5$, $\Delta T/\tau_v = 1.13$

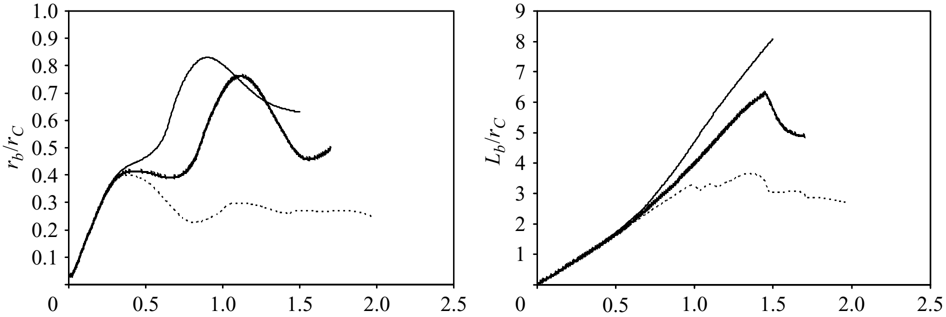

(c) $Re_\Gamma = 2 \times 10^5$, $\Delta T/\tau_v = 2.26$

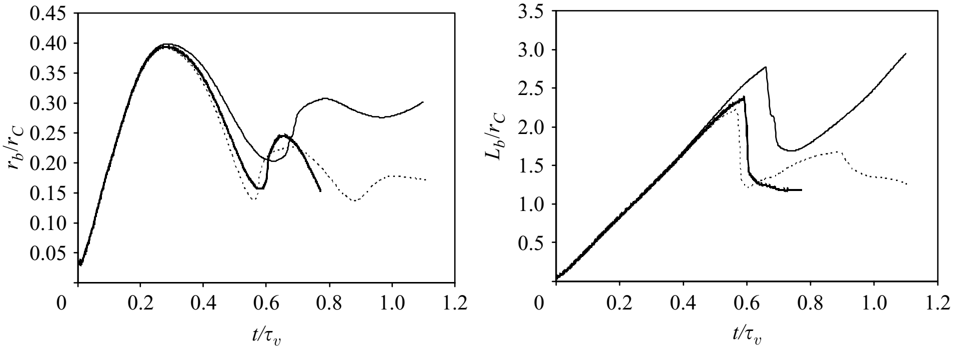

FIGURE 13. Bubble length and radius normalized by the vortex core radius during bubble growth at $Re_\Gamma = 2 \times 10^5$ or varying tensions and three rates of applied tension.

the bubble dynamics along the vortex axis couples with the radial flow. This coupling is illustrated in figures 14 and 15.

As in the cylindrical bubble computations, the radius of the bubble approaches an equilibrium value after the full extent of the tension has been applied, but the radius continues to oscillate with a period that is of the order of the vortex time scale, coupled with the vorticity time scale. Considering the wavelength of sound waves within the bubble, the speed of sound in the gas within the bubble is of order $400\,\mathrm{m\,s^{-1}}$, and the bubble length is of the order of 0.001–0.010 m. This would make the resonant frequency of the order of 40–400 kHz, which is much higher than the

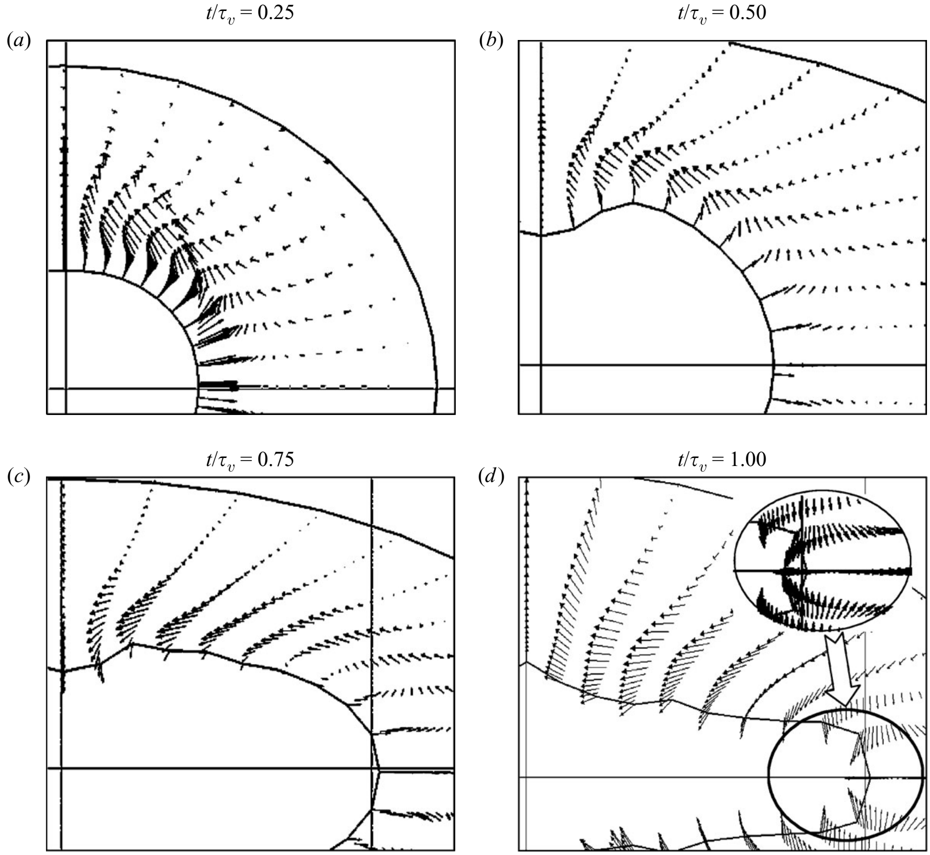

FIGURE 14. Flow fields near the bubble axial extent during growth with velocity vectors in a plane parallel to and intersecting the vortex axis. Vortex axis is in the horizontal direction. $Re_\Gamma = 2 \times 10^5$, $\sigma_C = -0.4$ and $\Delta T/\tau_v = 0.46$. The four images correspond to the four times labelled in figure 13(*a*).

observed frequency of the oscillating bubbles. But, there may be circumstances where the frequencies are more closely matched. The observed period of radial oscillations of axisymmetric and cylindrical bubbles is plotted in figure 7. The oscillation period of the axisymmetric bubble is approximately half that of the cylindrical bubble. While the domain size is smaller compared to the cylindrical calculations, the period is larger.

The sensitivity of the bubble dynamics to changes in the Reynolds number is illustrated in figure 12. A doubling of the Reynolds number produced significant differences to the shape history and dynamics of the bubbles, and this is also illustrated in figures 13 and 16, where the radius and length profiles for the growing bubbles at two different Reynolds numbers are compared. At higher Reynolds number, the overgrowth of the bubble is less than the case of lower Reynolds number, which is similar to the effect of longer time of applied tension. Thus, differences in the history of bubble growth are determined by differences in the spatial pressure gradient in the radial direction and in the temporal pressure gradients, resulting from the combination of both effects, which may not be scaled with Reynolds number. Note that a slower application of the pressure tension reduced the amplitude of radial bubble oscillation, as in the cylindrical bubble cases.

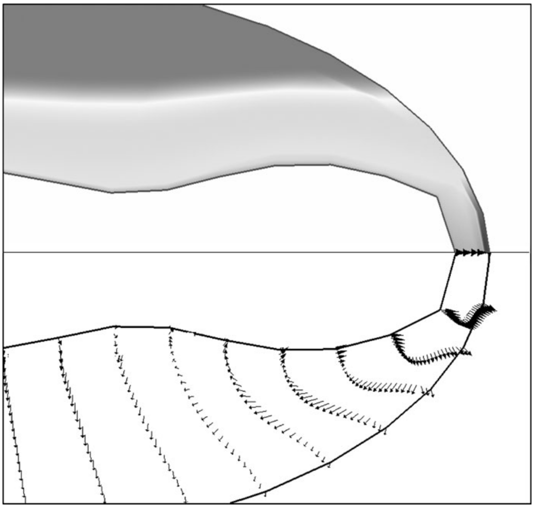

FIGURE 15. Velocity and pressure fields near the tip of the growing bubble for $Re_\Gamma = 4 \times 10^5$, $\sigma_C = -0.4$, $\Delta T/\tau_v = 0.23$, at time $t/\tau_v = 0.5$. The top half of the image shows relative pressure contours, and the bottom shows the local velocity in a plane parallel to and intersecting the vortex axis. Vortex axis is in the horizontal direction.

Also in the cylindrical bubble simulations, the growing bubble significantly modifies the circumferential velocity distribution around the bubble. Figure 17 presents the history of the circumferential velocity profile in a plane perpendicular to the vortex axis located at the centre of the elongating bubble for the cases shown in figure 12. Recall that for the cylindrical bubbles, the radial velocity at the bubble surface varies along its axial extent, and the data shown here are for particular planes intersecting the bubble axis. As the bubble pushes out the flow field, the vortex core is also pushed out with smaller maximum tangential velocity during bubble oscillation after tension is applied.

In the three-dimensional axisymmetric calculations, the bubble grows in both the radial and axial directions, and the bubble growth in the axial direction is not necessarily monotonic. The average rate of axial bubble growth along the vortex axis was computed, and this is compared to the experimental observations of Choi & Ceccio (2007) in figure 18. The axial growth rate $\dot{L}_b$ is normalized with the axial tension using $2\pi r_C \dot{L}_b / \beta \Gamma_O \sqrt{\sigma_C}$. The average normalized growth rate is in the range of 1.5 to 2.0 times larger than the experimentally observed growth rates. However, it should be noted that the experimentally observed bubbles were not exposed to a uniform pressure in the axial direction as they entered and exited the Venturi used to create the pressure rise and drop, while the calculations were conducted with a uniform pressure applied along the full axial extent of the domain boundary.

The elongated bubbles were allowed to grow to an aspect ratio of up to 10. Then, the average radius of the bubble was computed. These data were compared to the predicted envelope of possible equilibrium radii for very elongated bubbles, and are presented in figure 2. The computed radii are within the predicted envelope of the equilibrium radii, except for the case with the highest tension, when the bubble was not in equilibrium. As was the case of the cylindrical bubble calculations, the scaled radii are 2–3 times larger than the experimentally observed radii from Choi & Ceccio (2007). This is likely due to several factors. First, the external pressure is

(a) $Re_\Gamma = 4 \times 10^5$, $\Delta T/\tau_v = 0.23$

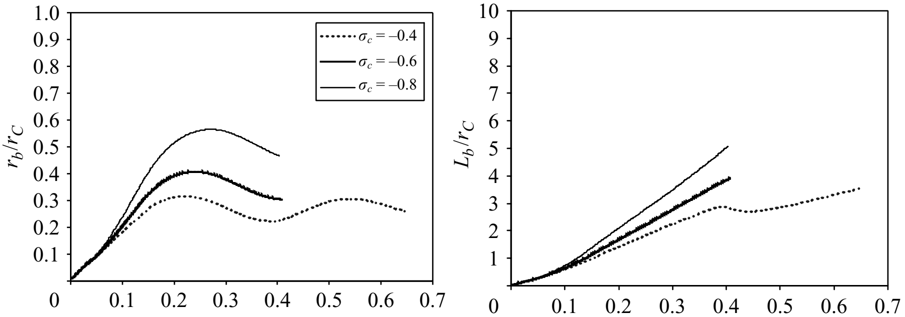

(b) $Re_\Gamma = 4 \times 10^5$, $\Delta T/\tau_v = 0.46$

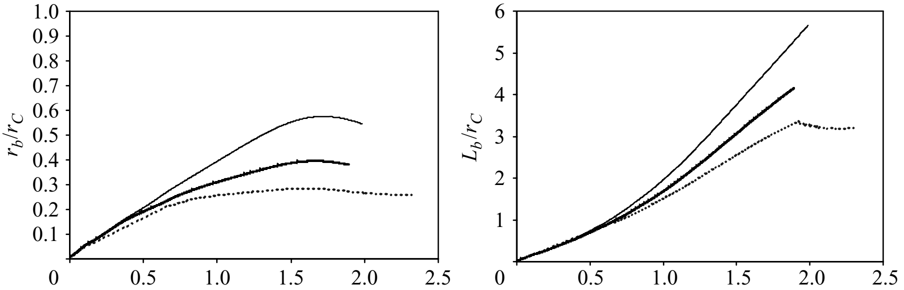

(c) $Re_\Gamma = 4 \times 10^5$, $\Delta T/\tau_v = 0.92$

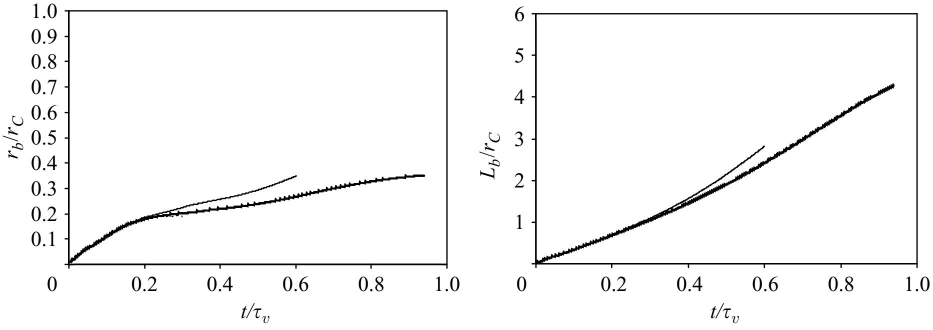

FIGURE 16. Bubble length and radius normalized by the vortex core radius during bubble growth at $Re_\Gamma = 4 \times 10^5$ or varying tensions and three rates of applied tension.

applied uniformly to the exterior of the computational domain for the axisymmetric simulations. But, in the experiment, there were finite pressure gradients along the axis of the vortex that led to significant pressure differences across the extent of the bubble. Second, the bubbles were constrained here to be axisymmetric, unlike the actual bubbles. Changes in the mean circumferential velocity near the bubble interface can result from surface waves and non-symmetric volume oscillations of the experimentally observed bubbles, and this in turn can change the mean pressures the bubbles experience. Also, recall that the computed bubbles had a finite circumferential velocity near their interface, which would lead to a larger bubble radius.

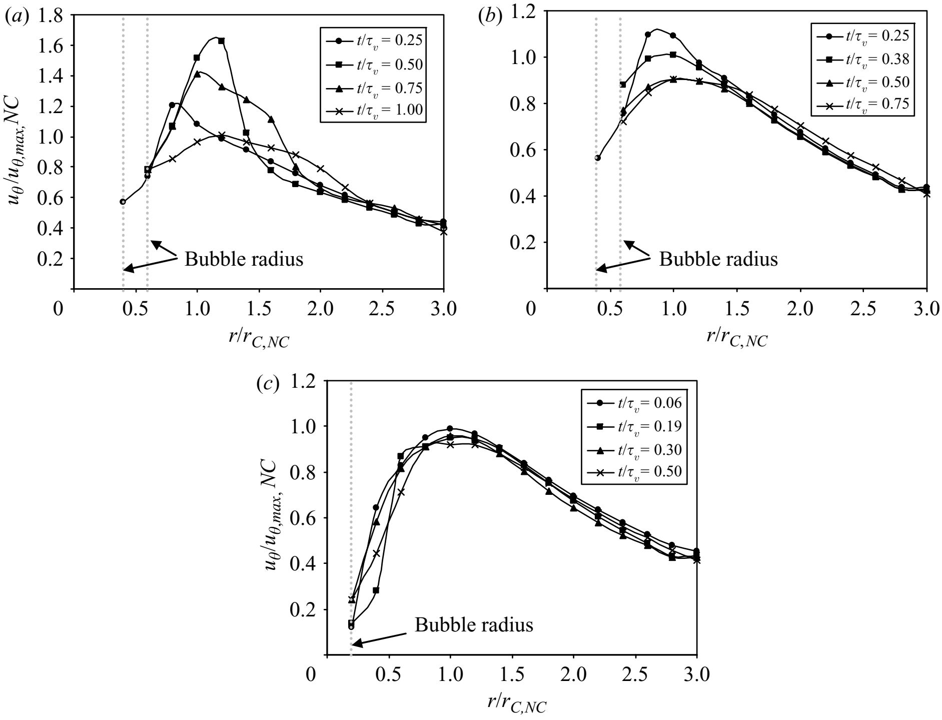

FIGURE 17. History of the circumferential velocity profile in a plane perpendicular to the vortex axis located at the centre of the elongating bubbles for the cases shown in figure 12. (*a*) $\sigma_C = -0.4$, $\Delta T/\tau_V = 0.46$, $Re_\Gamma = 2 \times 10^5$ (*b*) $\sigma_C = -0.4$, $\Delta T/\tau_V = 1.13$, $Re_\Gamma = 4 \times 10^5$ (*c*) $\sigma_C = -0.4$, $\Delta T/\tau_V = 0.23$, $Re_\Gamma = 4 \times 10^5$.

3.3. *Collapse of elongated vortex cavitation bubbles*

A series of bubbles were allowed to grow to a particular ratio of length to diameter. Then, an increase in the applied pressure (as shown in figure 3*b*) was imposed to initiate bubble collapse. Figure 19 shows the bubble volume history for two Reynolds numbers with $L_b/D_b = 2$. Pressure was applied to impose $\sigma_C = 0.3$. The bubble radii and length reduce, as expected. But, the bubbles also neck down and become pinched at their ends. This pinching can lead to bubble splitting. Figure 20 shows the radius and length history for the bubbles with aspect ratios ranging from 2 to 5 before collapse. Note that the time of collapse is much closer to the vortex time scale for these axisymmetric bubbles. Also, the splitting occurs after a collapse time that is often of the order of $\tau_v/2$, or half the period of oscillation.

Figure 21 shows the history of bubble collapse with flow field around bubble, leading to bubble splitting. Again, the radial and axial motions of the bubble are coupled through the flow field, especially at the ends of the bubble split. This is illustrated in figure 22 that presents a close-up of the velocity field for $t/\tau_v = 0.5$ along with the local static pressure, leading to splitting at both ends of the bubble. There are high-pressure regions at the bubble neck that can lead to splitting and the high pressures at the axial extents of the bubble can produce re-entrant jets (Choi & Chahine 2004, 2007). Figure 23 presents some close-up images of collapsing vortex cavitation bubbles as the flow pinches off the end of the elongated bubbles producing sub-bubbles. These smaller sub-bubbles can produce a noise pulse upon collapse in a

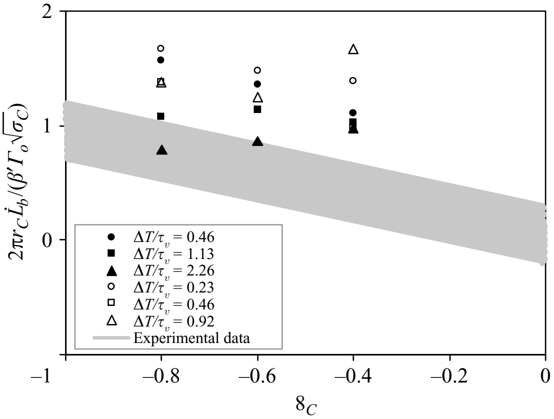

FIGURE 18. The growth rate of the bubble shape ratio in the axial direction as a function of the cavitation number at the vortex axis for varying rates of the applied tension and Reynolds number. Filled symbols ($Re_\Gamma = 2 \times 10^5$) and open symbols ($Re_\Gamma = 4 \times 10^5$). The shaded area is the experimental data for all conditions in Choi & Ceccio (2007).

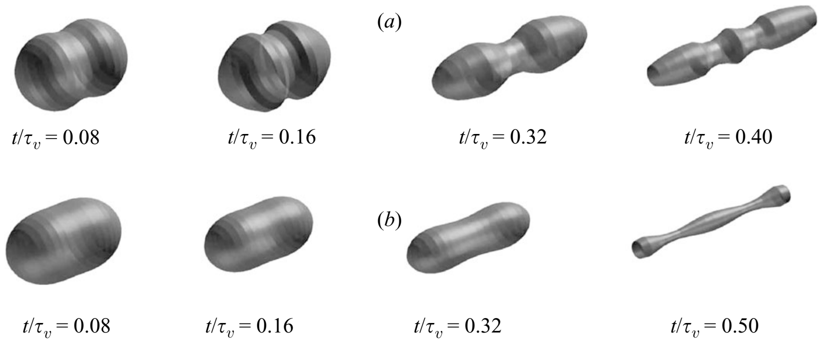

FIGURE 19. The volume history of elongated bubbles during collapse. The initial aspect ratio of the bubbles was $L_b/D_b = 2$, and a pressure was applied to impose $\sigma_C = 0.3$. (a) $Re_\Gamma = 2 \times 10^5$ and (b) $Re_\Gamma = 4 \times 10^5$.

manner similar to smaller near- spherical bubbles, as discussed by Oweis *et al.* (2004). The length scale that is the most important for the collapse of the sub-bubbles is their radius, which is similar to the radius of the elongated bubble.

4. Discussion and conclusions

The growth, splitting and collapse of two- and three-dimensional vortex cavitation bubbles were examined. The traditional scaling variables of vortex cavitation (i.e. Γ_O, r_C, σ_C, r_b) are important parameters that scale the basic features of the bubble inception, growth and collapse. However, the diameter of the elongated bubbles is not uniquely determined by the non-cavitating vortex properties and is influenced by the detailed conditions and processes at inception. Large nuclei (with near-zero critical tension), experiencing slowly applied tensions, will grow in a quasi-steady fashion, slowly displacing the fluid around the bubble. Small nuclei requiring a large tension to incept can grow explosively when the critical tension is reached. These bubbles rapidly displace the surrounding fluid, and the bubble radial dimension will

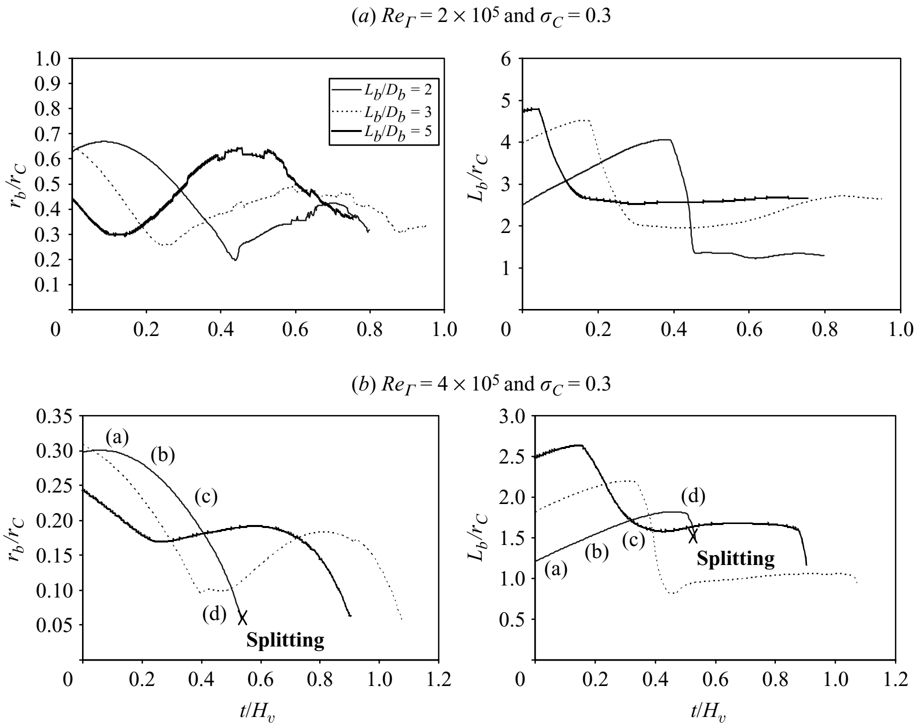

FIGURE 20. Bubble length and radius normalized by the vortex core radius during bubble collapse with various aspect ratios and (a) $Re_{\Gamma} = 2 \times 10^5$ and $\sigma_C = 0.3$ for $\Delta T/\tau_v = 1.13$ and (b) $Re_{\Gamma} = 4 \times 10^5$ and $\sigma_C = 0.3$ for $\Delta T/\tau_v = 0.46$.

overshoot the equilibrium radius. Once the radial growth of the bubble is arrested by the increasing radial pressure around the bubble, the bubble radius may diminish and ultimately oscillate around an equilibrium value. Or, the bubble radius may shrink so rapidly that the bubble can collapse or fission can occur. Thus, the influence of the nuclei distribution and the process leading to the dynamic reduction (or rise) of the core pressure are also important.

The two-dimensional analysis illustrates the basic mechanism responsible for the radial growth of the bubble to an equilibrium value through the redistribution of the flow around the bubble. The radial growth pushes fluid away from the rotational axis of the bubble, reducing its tangential velocity and thus increasing the pressure at the bubble interface. If the radial growth of the bubble is slow, the bubble can reach a new equilibrium radius without significant overshoot. However, if the growth of the bubble is rapid (possibly due to the inception of a strong nucleus under high tension), the bubble radius will strongly overshoot the equilibrium value. This will lead to strong radial oscillations of the bubble. The dynamics of these radial bubble oscillations are scaled with the non-cavitating vortex time scale τ_v.

However, the two-dimensional bubble calculations do not capture other important features of the bubble dynamics such as the presence of circumferential perturbations on the bubble interface. Moreover, actual bubbles are three-dimensional and grow and collapse in the axial as well as the radial direction. The three-dimensional calculations reveal important interactions between the radial and axial motions of the growing and collapsing cavitation bubbles. The growth and collapse of these bubbles

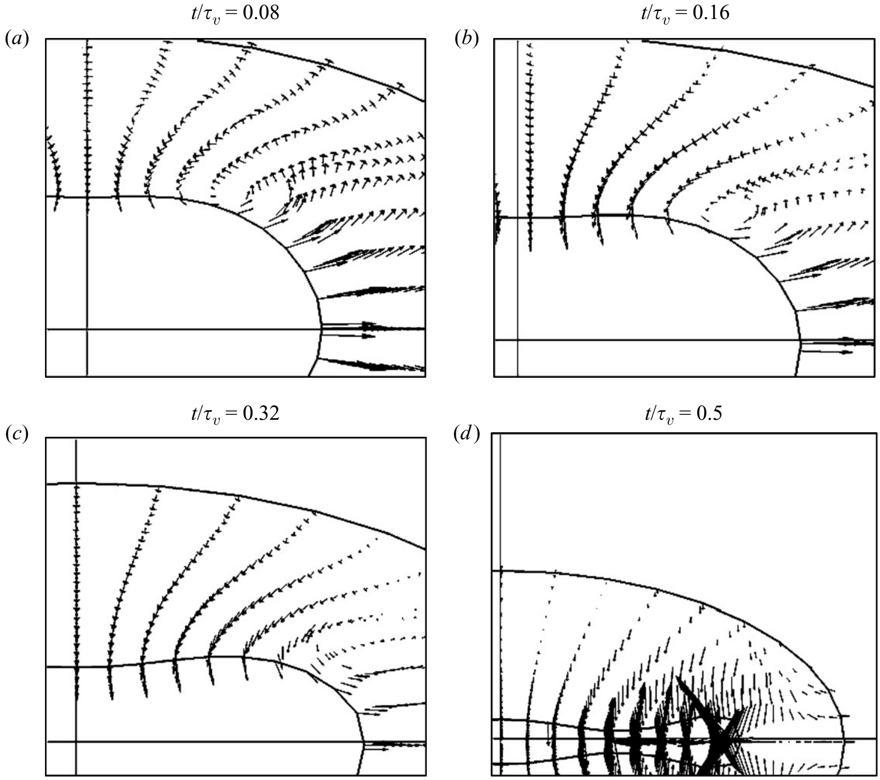

FIGURE 21. Flow fields near the bubble axial extent during collapse with velocity vectors in a plane parallel to and intersecting the vortex axis. Vortex axis is in the horizontal direction. $Re_\Gamma = 4 \times 10^5$, $L_b/D_b = 2$, $\sigma_C = 0.3$. The four images correspond to the four times labelled in figure 20(b).

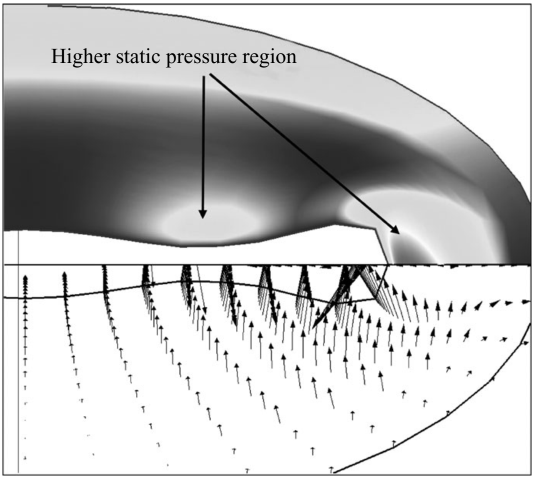

FIGURE 22. Velocity and pressure fields near the tip of the collapsing bubble illustrating the process responsible for splitting. Vortex axis is in the horizontal direction; $t/\tau_v = 0.5$, $Re_\Gamma = 4 \times 10^5$, $L_b/D_b = 2$ and $\sigma_C = 0.3$

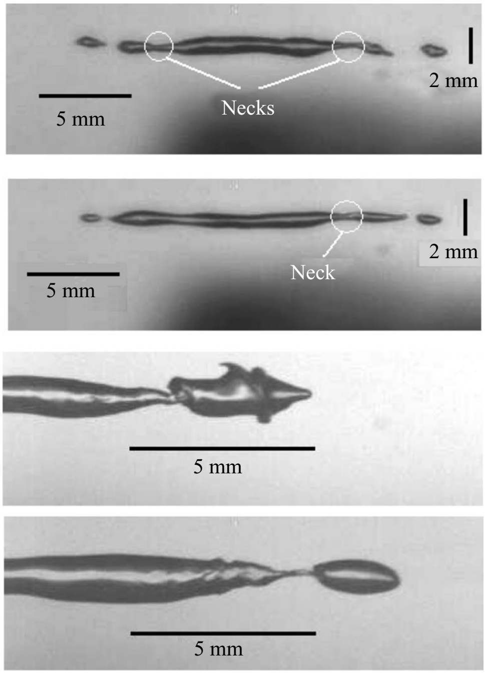

Figure 23. Images of collapsing vortex cavitation bubbles that illustrate the ‘pinch-off’ of sub-bubbles. Note that after a single bubble forms on one end, the pinching process continues and other bubbles may be formed.

exhibit complex volume time histories, and radial flows induced by the expanding of collapsing bubbles could lead to changes in pressures and flow at the axial extent of the bubbles. Bubbles would undergo fission upon collapse through the production of sub-bubbles at the extreme ends of the original elongated bubble. And, since the radius of the elongated bubble is much smaller than its length, the bubble can collapse in the radial direction much sooner, leading to splitting (also see Choi *et al.* 2004, 2007 for a further discussion of vortex bubble splitting). The computed bubble radii and axial growth rates are similar to those observed by Choi & Ceccio (2007), and are typically within a factor of 2. However, both the experimental observations and the results presented here indicate that the growth, dynamics and collapse of vortex cavitation bubbles are quite sensitive to the underlying flow parameters, such as the Reynolds number and the rate and spatial distribution of the applied tension or collapse pressure. This makes the prediction of vortex cavitation dynamics both a rich and challenging problem.

This work was supported by the Office of Naval Research under grant number N00014-03-1-0430, Dr K.-Han Kim, Program Manager.

REFERENCES

Arabshahi, A., Taylor, L. K. & Whitfield, D. L. 1995 UNCLE: toward a comprehensive time accurate incompressible Navier-Stokes flow solver. *AIAA-95-0050,* Reno, NV.

Arndt, R. 2002 Cavitation in vortical flow. *Annu. Rev. Fluid Mech.* **34**, 143–175.

Arndt, R. & Keller, A. 1992 Water quality effects on cavitation inception in a trailing vortex. *J. Fluids Engng* **114**, 430–438.

CHAHINE, G. L. 1995 Bubble interactions with vortices. In *Vortex Flows* (ed S. Green), vol. 30, pp. 783–823. Kluwer Academic.

CHESNAKAS, C. & JESSUP, S. 2003, Tip vortex induced cavitation on a ducted propulsor. In *Proceedings of 4th ASME-JSME Joint Fluids Eng. Conf.*, FEDSM2003-45320, Honolulu, Hawaii.

CHOI, J. & CECCIO, S. L. 2007 Dynamics and noise emission of vortex cavitation bubbles. *J. Fluid Mech.* **575**, 1–26.

CHOI, J. K. & CHAHINE, G. L. 2004 Noise due to extreme bubble deformation near inception of tip vortex cavitation. *Phys. Fluids* **16** (7), 2411–2418.

CHOI, J. K. & CHAHINE, G. L. 2007 Modeling of bubble generated noise in tip vortex cavitation inception. ACTA Acoustica United with Acustica, *J. Eur. Acoustics Assoc.* **93**, 555–565.

CHOI, J. K., HSIAO, C.-T. & CHAHINE, G. L. 2004 Tip vortex cavitation inception study using the Surface Averaged Pressure (SAP) model combined with a bubble splitting model. In *Proceedings of 25th Symposium on Naval Hydrodynamics,* Canada.

FRANC, J.-P. AND MICHEL, J.-M., 2004, *Fundamentals of Cavitation.* Springer.

HSIAO, C.-T. & CHAHINE, G. L. 2001 Numerical simulation of bubble dynamics in a vortex flow using Navier-Stokes computations and moving Chimera grid scheme. In *Proc. CAV2001*, Pasadena, CA.

HSIAO, C.-T. & CHAHINE, G. L. 2004 Prediction of tip vortex cavitation inception using coupled spherical and nonspherical bubble models and Navier–Stokes computations. *J. Marine Sci. Tech.* **8**, 99–108

HSIAO, C.-T. & CHAHINE, G. L. 2005 Scaling of tip vortex cavitation inception noise with a bubble dynamics model accounting for nuclei size distribution. *J. Fluids Engng* **127**, 55–65.

HSIAO, C.-T., CHAHINE, G. L. 2008 Numerical study of cavitation inception due to vortex/vortex interaction in a ducted propulsor. *J. Ship Res.* **52**, 114–123.

IYER, C. O. & CECCIO, S. L. 2002 The influence of developed cavitation on the flow of a turbulent shear layer. *Phys. Fluids* **14** (10), 3414–3431.

KATZ, J & O'HERN, T. J., 1986 Cavitation in large scale shear flow. *J. Fluids Engng.* **108**, 373–376.

KEDRINSKII, V. K. 2005 *Hydrodynamics of Explosion: Experiments and Models.* Springer.

O'HERN, T. J. 1990 An experimental investigation of turbulent shear flow cavitation. *J. Fluid Mech.* **215**, 365–391.

OWEIS, G. & S. L. CECCIO 2005 Instantaneous and time averaged flow fields of multiple vortices in the tip region of a ducted propulsor. *Exp. Fluids* **38**, 615–636.

OWEIS, G. F., CHOI, J. & CECCIO, S. L. 2004 Dynamics and noise emission of laser induced cavitation bubbles in a vortical flow field. *J. Acoust. Soc. Am.* **115** (3), 1049–1058.

OWEIS, G., FRY, D., CHESNAKAS, C. J., JESSUP, S. D. & CECCIO, S. L. 2006*a* Development of a tip-leakage flow: Part 1 – the flow over a range of Reynolds Numbers. *J. Fluids Engng* **128**, 751–764.

OWEIS, G., FRY, D., CHESNAKAS, C. J., JESSUP, S. D. & CECCIO, S. L. 2006*b* Development of a tip-leakage flow: Part 2 – Comparison between the ducted and un-ducted rotor. *J. Fluids Engng* **128**, 765–773.